

Structure evolution of spinel Fe- M^{II} ($M = \text{Mn}, \text{Fe}, \text{Co}, \text{Ni}$) ferrite in CO hydrogenation



Bianfang Shi^{a,b,*}, Zhengpai Zhang^a, Binbin Zha^a, Da Liu^a

^a State Key Laboratory of Chemical Engineering, School of Chemical Engineering, East China University Science and Technology, Shanghai 200237, China

^b 985 Instrument Analysis Center, School of Chemical Engineering, East China University Science and Technology, Shanghai 200237, China

ARTICLE INFO

Keywords:

CO hydrogenation
Fischer-Tropsch synthesis
Syngas
Ferrite

ABSTRACT

The CO hydrogenation via the Fischer-Tropsch reaction (FTO) has been carried out over spinel bimetallic Fe- M^{II} ($M = \text{Fe}, \text{Mn}, \text{Co}, \text{Ni}$) ferrite. The catalytic performance shows that Fe-Mn ferrite has the highest lower olefin selectivity of 54.5%, while Fe-Ni ferrite has the highest CH_4 selectivity. The initial structure of the ferrite is characterized by scanning electron microscopy, energy-dispersive spectrometry, X-ray diffraction (XRD), and Raman spectroscopy. The structure evolution was also characterized by *in situ* XRD. The results revealed that the doping of a second metal decreases the grain size and microsphere size. Also, the doping of Mn promotes the reduction of $\text{Mn}_x\text{Fe}_{3-x}\text{O}_4$ phase to $\text{Mn}_x\text{Fe}_{1-x}\text{O}$ phase; however, further reduction of Fe^{2+} in the $\text{Mn}_x\text{Fe}_{1-x}\text{O}$ phase is inhibited, while the doping of Co and Ni favors the reduction of $\text{M}_x\text{Fe}_{3-x}\text{O}_4$ to alloy phase and metal phase. $\chi\text{-Fe}_5\text{C}_2$ phase was found for all the spent catalysts, a small $\epsilon\text{-Fe}_2\text{C}$ phase was also detected from spent Fe-Mn ferrite, and $\theta\text{-Fe}_3\text{C}$ determined to be the principle carbide for the spent Fe-Co sample.

1. Introduction

Lower olefins [ethylene, propylene, and butylenes ($\text{C}_2\text{-C}_4$)] are the most essential and primary industrial materials for the production of plastic, rubber, film, etc. [1]. Traditionally, lower olefins are produced by steam cracking of naphtha, dehydrogenation of hydrocarbons, or as by-products of oil-refining processes [2]. However, the oil-reserve crisis has gradually become a heated issue. As is well known, Asia's coal reserves are much greater than those of gas and oil [3]. It is therefore conceivable that developing coal-based syngas to produce lower-olefin products has crucial strategic significance. The conversion of syngas directly to lower-olefin products via Fischer-Tropsch synthesis (FTO), as a direct route without intermediate steps, has proved to be an alternative process to increasing olefin output [4,5].

The advance in FTO has been recently reviewed by Torres Galvis et al. [6]. Generally, the development of high-performance catalysts is still of paramount importance. In the past several decades, the Fischer-Tropsch catalysts based on group-VIII metals such as Fe, Co, Ru, Rh, and Ni have been extensively investigated [7–11]. Iron-based catalysts are widely used for FTO as they are cheap and widely available. They also have high selectivity for olefin and low selectivity for methane, as well as the feasibility of lowering the H_2/CO ratios derived from coal or biomass [12,13]. Moreover, they exhibit high activity for both Fischer-Tropsch synthesis (FTS) and Water-Gas Shift (WGS) reactions [6,14].

However, there are still some areas of dispute in the reaction process when iron-based catalysts are used in CO hydrogenation, such as the phase transformation, reaction mechanism, and active phases. Furthermore, the performance of iron-based catalysts can be significantly affected by many factors, such as supports, promoters, the addition of a second metal, etc.

Many studies have shown that the use of bimetallic catalysts with generated synergistic geometric and electronic effects can improve FTS performances (activity, selectivity, and stability) of Fe-based catalysts. Typical iron-FTS bimetallic Fe- M ($M = \text{Co}, \text{Ni}, \text{and Mn}$) catalysts have shown excellent performance for FTS [15–17]. Fe-Co catalysts are efficient in producing $\text{C}_2\text{-C}_4$ olefins and are stable under a CO/H_2 atmosphere, with only few carbides detected [15,18]. Ni is a well-known methanation catalyst, so it is expected that it would have a negative influence on the O/P ratio [16,17]. Mn can decrease the methane selectivity and promote the formation of olefin [19]. However, in a previous study, most of the precursor is Fe_2O_3 , which is obtained by calcination in air. In addition, the catalysts are mainly prepared by co-precipitation. In fact, co-precipitation is the preferred choice for most studies owing to the simple preparation conditions and operational process; however, mixture by co-precipitation is not homogenous enough, and it is difficult to control the shape and size of the final products. In addition, FT is viewed as a structure-sensitive reaction, and the shape and size of the catalysts have significant effects on catalytic

* Corresponding author at: 985 Instrument Analysis Center, School of Chemical Engineering, East China University Science and Technology, Shanghai 200237, China.
E-mail address: Shibf@ecust.edu.cn (B. Shi).

performance [20]. In recent years, Fe₃O₄ microspheres prepared by the solvothermal method have been used as FTO catalysts [21–23]. The preparation process is simple, environmentally friendly, and the grain size can be adjusted. In addition, the support-free Fe₃O₄ microspheres can overcome any strong metal-support interaction. In this paper, the second metals were doped using one-pot solvothermal method and a series of Fe-based spinel Fe-M^{II} (M = Mn, Fe, Co, Ni) ferrites obtained. The ferrites were used to direction-convert syngas to lower olefins, and the key is focusing on the effect of the doping of second metal on the performance of the reduction and CO hydrogenation.

2. Experiment

2.1. Catalyst preparation

Fe₃O₄ ferrite was prepared through a solvothermal reaction [24,25]. Fe-M (M = Mn, Co, Ni) was prepared as follows: Using Fe-Mn ferrite as an example, FeCl₃·6H₂O (analytical reagent (AR), SinoPharm, China) and MnCl₂·4H₂O (AR, SinoPharm, China) were dissolved in ethylene glycol to form a clear solution; the total initial metal-ion concentration was 0.1 M. The nominal content of second doping metal is 33.3% relative to the total metal ions during solvothermal synthesis. After stirring the solution for 1 h, sodium acetate was added, and the mixture was vigorously stirred for 1 h. The mixture was then sealed in a Teflon[™]-lined stainless-steel autoclave (100 mL capacity). The autoclave was heated and maintained at 200 °C for 8 h, and allowed to cool to room temperature. The products were washed several times, separately with ethanol and with water. They were then collected by magnet and dried at room temperature under vacuum and kept in a vacuum oven. The other two Fe-M (M = Co, Ni) ferrites were prepared using the same procedure. The actual content of second doping metal is denoted as M (%) determined by ICP and EDS.

2.2. Characterization

2.2.1. Scanning electron microscopy

The morphologies of the samples and the elemental concentrations of the catalysts, as well as elemental distributions, were studied using scanning electron microscopy (SEM) and energy-dispersive X-ray (EDS) spectroscopy. The mean microsphere size was obtained from SEM images. SEM equipped with EDX spectroscopy was performed using a high-resolution field-emission SEM instrument (NOVA Nano SEM450, FEI/ThermoFisher Scientific, USA) under the scanning electron (SE) mode. The accelerating voltage was 3 kV with a working distance of 5 mm.

2.2.2. Inductively coupled plasma spectrophotometer

The element contents of samples were obtained by Inductively Coupled Plasma spectrophotometer (ICP) (Perkin Elmer Avio 500). The 0.10–0.15 g of sample was dissolved into 3 mL of concentrated HNO₃ (65%) and diluted into 50 mL with deionized water. Subsequently, the solutions were performed on the ICP.

2.2.3. X-ray powder diffraction

X-ray powder diffraction (XRD) analysis was carried out on a diffractometer (D8 Advance, Bruker Corp., USA). Cu K α radiation ($\lambda = 1.5406$) obtained at 40 kV, and 40 mA was used as the X-ray source. The XRD patterns used to calculate the grain size and lattice parameters of the fresh catalyst were obtained with 0.02° as one step, at a scanning rate of 0.24°/min. The intensity of the highest peak is more than 10,000 counts per second (cps). The grain size of the microspheres was calculated with Scherrer's equation using the Fe₃O₄(311) peak at $2\theta = 35.5^\circ$. The lattice parameters were calculated using the Rietveld refinement software TOPAS (Bruker Corp., USA). The XRD patterns of the spent catalyst were obtained with 0.02° as one step, at a scanning rate of 3°/min.

The *in situ* XRD experiments in a H₂ atmosphere were carried out on the same instrument in a reaction chamber (XRK-900, Anton Paar GmbH, Germany). In each XRD experiment, diffraction patterns of the catalyst were recorded within a 2θ range of 10°–80°, at a scanning rate of 10°/min, and the sample was heated in a flow of 3% H₂ in Ar (50 mL/min) up to 623 K at a rate of 5 K/min for 5 h. During this process, the XRD patterns were collected at the pre-specified temperatures.

2.2.4. H₂-temperature-programmed reduction (H₂-TPR)

Prior to the experiment, the sample (50 mg) was purged with Ar (30 mL·min⁻¹) at 428 K for 1 h so that the physically adsorbed H₂O could be removed from the samples. The H₂-TPR experiments were performed using a fixed-bed micro-reactor connected with a thermal conductivity detector (TCD). The temperature was ramped from 303 to 398 K at a rate of 20 K·min⁻¹ for 5 min, and the temperature was then ramped to 1098 K at a rate of 10 K·min⁻¹ in a 10% H₂/He flow of 50 mL·min⁻¹.

2.2.5. Raman

The laser Raman spectrometer (LabRAM HR, Horiba J.Y., Japan) was equipped with a high-grade microscope (Leica Camera AG, Germany; long working distance objective lens, 50×). The sample was placed in the *in situ* cell under the protection of Ar at a flow rate of 30 mL/min. Raman measurements were performed on different sample spots irradiated by a visible 514.5-nm Ar⁺-ion laser. The single silicon crystal was used for position correction. The confocal hole was set to 200 mm for all tests. The attenuator (DO.6) was used for the tests to avoid signal overflow and sample degradation. The exposure time was set to 40 s for each spectrum. The scattered light was collected at 180° (back-scattering plane) and detected by a deep-depleted, thermoelectrically cooled, charge-coupled-device (CCD) array detector (1024 × 256 pixels, 26 mm in size).

2.3. Catalytic performance

CO hydrogenation was performed in a stainless-steel, continuous, fixed-bed micro-reactor with a length of 450 mm, inner and external diameter of 6 mm and 9 mm. The catalyst precursor was first reduced at 623 K with H₂ (30 mL·min⁻¹) for 5 h. Ahead of the reaction, syngas at 2.0 MPa was then introduced into the reaction system. The reaction temperature was monitored by a thermocouple inserted into the catalyst bed, and a time-on-stream of 20 h was taken for each measurement. Catalyst screening experiments were usually measured under the following conditions: 533 K; gas hourly space velocity (GHSV) of 4000 h⁻¹; H₂/CO ratio = 1; 25 mg catalyst diluted with 75 mg SiC. The blank test was implemented using SiC, and a less than 0.45% conversion of CO was detected under the same reaction conditions. The products were analyzed using an online gas chromatograph (GC2060 Shanghai Ruimin, China).

3. Results and discussions

3.1. Catalytic performance of Fe-M ferrite

The catalytic performance results of the Fe-M catalyst in CO hydrogenation is shown in Table 1. After adding the Fe-M catalyst, the CO conversion ratio ranged from 3.3 to 7.0%, implying that the CO hydrogenation is catalyzed. However, the addition of a second metal decreased the conversion slightly, although Fe-Mn, Fe-Co, and Fe-Ni catalysts may expose less active sites for reaction. Mn did not exhibit FTO activity alone. Although Co and Ni exhibit activity for the FT reaction, the activity of Co and Ni for the FTO reaction is not as high as that of Fe [26]. The Fe-Co catalyst activity was also slightly lower than Fe₃O₄.

The pure Fe₃O₄ catalyst provides 17.3% selectivity of CH₄ and 27.5% selectivity of C₂-C₄ olefins, as well as 16.7% selectivity of CO₂.

Table 1
FTO performance over Fe-M catalysts.

Catalyst	Fe ₃ O ₄	Fe-Mn	Fe-Co	Fe-Ni
CO conversion (%)	7.0	5.4		5.3
Selectivity, carbon based (%)				
CH ₄	17.3	12.7		27.3
C ₂ ⁼	5.4	10.2		3.4
C ₂ [°]	9.4	4.5		14.6
C ₃ ⁼	15.6	18.8		12.9
C ₃ [°]	4.3	3.1		6.1
C ₄ ⁼	6.5	11.7		4.8
C ₄ [°]	9.2	3.8		8.5
C ₂ -C ₄ ⁼	27.5	40.7		21.0
C ₅ ⁺	15.6	10.0		9.7
CO ₂	16.7	25.2		10.2
C ₂ -C ₄ ⁼ Without CO ₂	33.0	54.5		23.4
O/P (C ₂ -C ₄)	1.2	3.6		0.7

Catalysts: 25 mg sample + 75 mg SiC.

Reaction conditions: 533 K; 2.0 MPa; GHSV, 4000 h⁻¹; H₂/CO, 1:1.

Meanwhile, the molar ratio of olefin to paraffin (denoted O/P) in the C₂-C₄ range hydrocarbons is as low as 1.2. For Fe-Mn catalyst, the CH₄ selectivity decreases to 12.7%, while C₂-C₄ olefin selectivity increases to 40.7% and CO₂ selectivity increases to 25.2%. This means that Fe-Mn enables suppression of the formation of CH₄, while increasing the selectivity of light olefin and CO₂. In contrast, for Fe-Co and Fe-Ni, the CH₄ selectivity increased to 27.3% and 32.8%, respectively, and the C₂-C₄ olefin selectivity dropped to 21.0% and 7.4%, respectively. The selectivity to CO₂ decreased to 10.2% and 8.0%, respectively. The systematic characterizations are provided to clarify the difference of catalytic performance and structure evolution in the following text.

3.2. Structure of fresh Fe-M ferrite

Fig. 1 displays the SEM images of the fresh ferrite. Generally, as can be seen, the Fe₃O₄ ferrite exhibits a spherical morphology that is uniform and monodisperse and composed of many tiny nanocrystals. For other Fe-M (M = Mn, Co, Ni) ferrites, the particles still maintain spherical morphology, but the microspheres are no longer monodisperse, particularly for Fe-Ni ferrite. In addition, the particle size of Fe-M (M = Mn, Co, Ni) ferrites (120–250 nm) were smaller than that of Fe₃O₄ (390 nm). The ICP results (Table 2) indicate the actual doping content of elemental Mn was only 10.4% for Fe-Mn ferrite, while the doping contents of Co and Ni are 29.4% and 32.8%, respectively. The actual doping content for the second metal (M = Mn, Co, Ni) is lower than the nominal content (33.3%). Mn atoms were found to have more difficulty in penetrating the spinel structure compared with other metals. By ICP, we also obtained the content of remnant Na in the samples and found that the remnant content of Na was so little that the influence of remnant Na on the catalytic performance can be ignored in this work.

XRD patterns of the as-prepared ferrite are shown in Fig. 2. The diffraction peaks at 18.3°, 30.1°, 35.5°, 43.1°, 53.5°, 57.0°, and 62.6° [Fig. 2(b)] could be assigned to the cubic inverse spinel Fe₃O₄ (JCPDS Card No. 75-1609). The other three patterns of Fe-M (M = Mn, Co, Ni) were similar to those of Fe₃O₄, indicating the successful synthesis of spinel M^{II}_xFe_{3-x}O₄ (M = Mn, Co, Ni) by the solvothermal method. The XRD peaks were collected at a slow scanning rate until the highest peak counts were above 10,000 cps. Using the TOPAS software, the crystal size and lattice parameters were calculated, and are listed in Table 2. Compared to pure Fe₃O₄, the lattice parameter of Fe-M (M = Mn, Co, Ni) shows a slight change, indicating that the second metal was successfully doped into the lattice structure. The crystal size of pure Fe₃O₄ was 15.8 nm, whereas the mean crystal size was between 6.4 and 10.5 nm calculated by Scherrer's formula, smaller than that of Fe₃O₄ ferrite.

As stated above, the CO conversion decreased with the addition of the second metal. Moreover, the catalytic performance may be affected

by the Fe-active sites, and the actual amount of Fe in the catalysts and the microsphere size may influence the number of active sites and the CO conversion.

To obtain more in-depth information with respect to the local structure, the Raman spectra were recorded at room temperature (Fig. 3). Three obvious first-order Raman modes—E_g, T_{2g}, and A_{1g}—are shown at approximately 300, 460, and 670 cm⁻¹, respectively, which closely match those reported earlier for Fe₃O₄ [27]. The peaks centered at 334 cm⁻¹ (E_g) represent symmetric and asymmetric bending of Fe-O bonds, that at 473 cm⁻¹ (T_{2g}) is due to the asymmetric stretching of Fe-O bonds, and that at 635 cm⁻¹ (A_{1g}) is attributed to the symmetric stretching of O atoms along Fe-O bonds [28]. The strongest peaks related to the A_{1g} mode of Fe₃O₄, Fe-Mn, Fe-Co, and Fe-Ni were centered at 684, 611, 677, and 674 cm⁻¹, respectively. There is an obvious shift to lower wavenumber for other ferrites compared with Fe₃O₄ because of the M-O vibrations (M = Mn, Co, Ni). These results further indicate that the second metal is incorporated into the lattice matrix to form M-O bonds with short-range order. These effects are commonly ascribed to the decrease of particle size, which directly affects the force constants and vibration amplitudes of the nearest-neighboring bonds [29].

3.3. Reduction behavior of Fe-M ferrite

The reduction behavior was investigated by H₂-TPR, with the results shown in Fig. 4, and *in situ* XRD, with the results shown in Fig. 5. H₂-TPR revealed that Fe-M (M = Mn, Co, Ni) ferrites were easier to reduce by H₂ than pure Fe₃O₄. The doping of Mn slightly favors a decrease of the initial reduction temperature; nevertheless, the catalyst was not completely reduced at 1073 K. However, in contrast, pure Fe₃O₄ was completely reduced. Moreover, the reduction process of Fe-Mn at temperatures higher than 900 K occurred much more slowly than for the other three catalysts, because Fe and Mn can form a Mn_xFe_{1-x}O solid-solution phase that can suppress the reduction of Mn_xFe_{1-x}O to the Fe[°] phase. It is obvious that Fe-Co and Fe-Ni were much easier to reduce. Fe-Co ferrite was totally reduced at 887 K, while Fe-Ni ferrite was totally reduced at 822 K. While the doping of a second metal can increase the dispersion of Fe₃O₄ and decrease the grain size, the catalysts can form Fe-Co or Fe-Ni alloys, which can decrease the reduction temperature [30]. The reduction process was further studied by *in situ* XRD under a H₂ atmosphere. Some previous studies [31] have reported that Mn could suppress the reduction of the Fe₃O₄ catalyst.

To further investigate the phase evolution during the reduction process, the Fe-M ferrite was characterized by *in situ* XRD under a H₂ atmosphere (Fig. 5). For all the catalysts, the spinel structure M^{II}_xFe_{3-x}O₄ (M = Fe, Mn, Co, Ni) was observed at room temperature. With increasing temperature, the diffraction peaks became sharper and narrower, indicating the growth of nanocrystals in the H₂ atmosphere. However, the phase transformation was quite different among these catalysts. There was no new phase emergent below 350 °C for Fe₃O₄ [Fig. 5(a)]. However, after reduction at 350 °C for 1 h, the Fe[°] phase appeared. With increasing time, the amount of Fe[°] also increased, while no FeO peak could be observed. It seems that Fe₃O₄ could be directly reduced to Fe[°], and the formation of FeO phase was not observed. Another possibility is that the transformation rate of intermediate FeO to Fe[°] is too fast to be detected [32]. The result suggests that the phase transformation in the bulk regions for the Fe₃O₄ catalyst in a H₂ atmosphere follows the order Fe₃O₄ → FeO → Fe[°]. For an Fe-Mn ferrite catalyst [Fig. 5(b)], similar to Fe-Mn ferrite, no significant structural change could be initially found with increasing reduction temperature. After reduction at 350 °C for 2 h, the diffraction peaks of Mn_xFe_{1-x}O emerged, and, after reduction for 5 h, the catalyst was composed of Mn_xFe_{3-x}O₄ and Mn_xFe_{1-x}O phases. Meanwhile, no Fe[°] phase was detected, which could be caused by the doping of Mn, which can inhibit Mn_xFe_{1-x}O phase, further reducing to Fe[°] and MnO, and thereby stabilizing the active phase [33]. The reduction tendency of the Fe-Co catalyst [Fig. 5(c)] was found to be quite different from that of Fe₃O₄

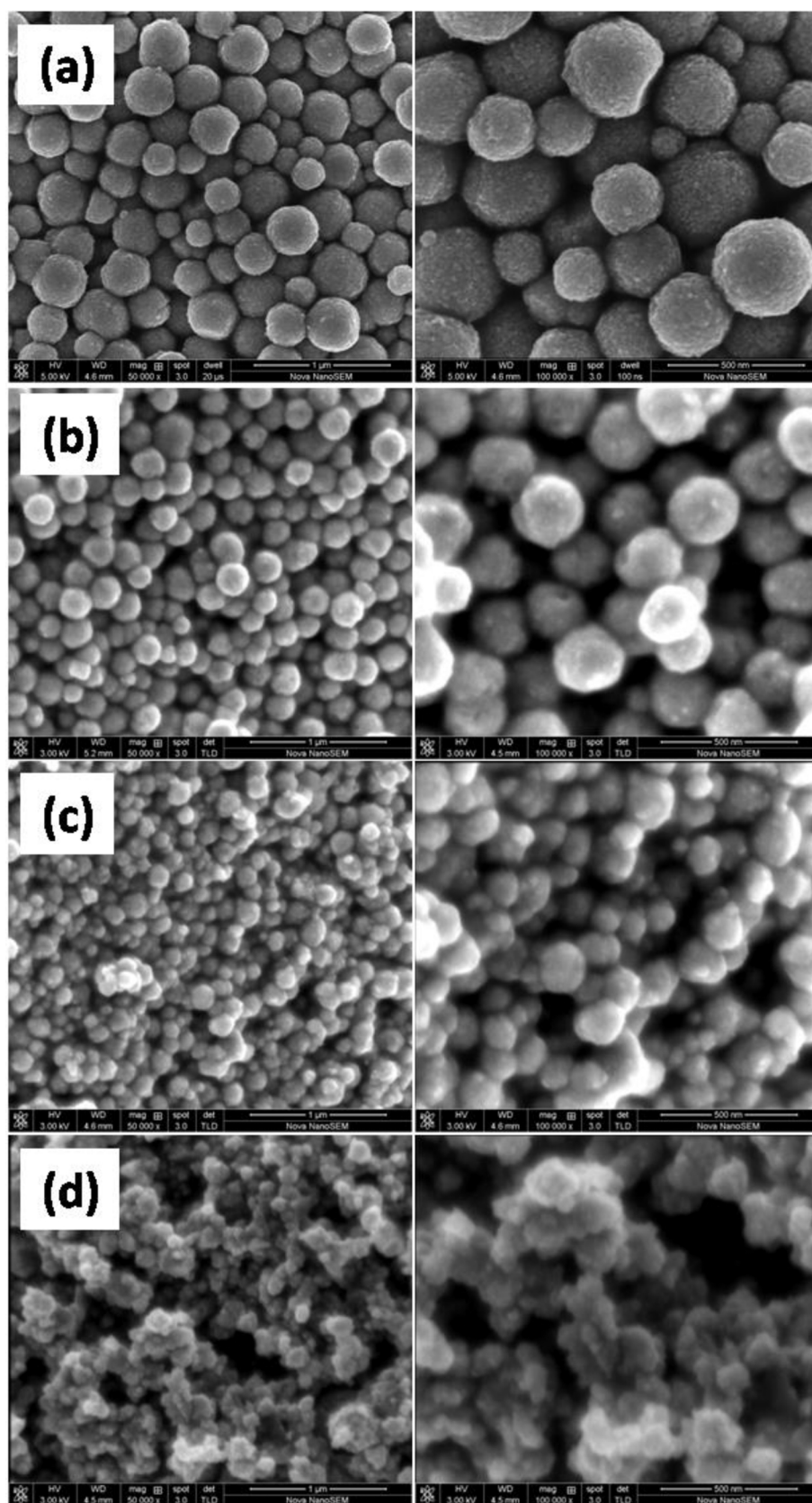


Fig. 1. SEM images of a series of ferrite: (a) Fe₃O₄; (b) Fe-Mn; (c) Fe-Co; (d) Fe-Ni.

Table 2
Structural parameters and composition of Fe-based microspheres.

Sample	Mean size of microspheres (nm)	Crystal size (nm)	Lattice parameters (Å)	M (%) by EDS	M(%) by ICP
Fe ₃ O ₄	390	15.8	8.3898	0	0
Fe-Mn	250	10.5	8.3981	10.5	10.4
Fe-Co	140	8.4	8.4033	25.3	29.4
Fe-Ni	120	6.4	8.3817	27.8	32.8

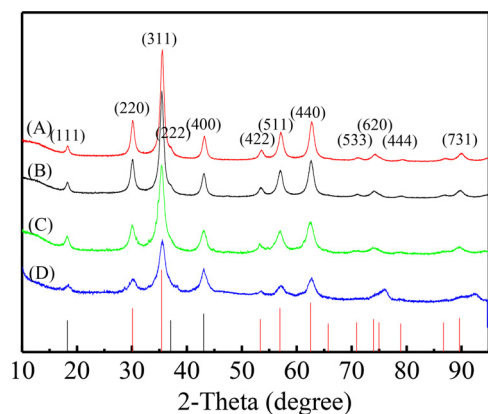


Fig. 2. XRD patterns of ferrites: (A) Fe₃O₄; (B) Fe-Mn; (C) Fe-Co; (D) Fe-Ni.

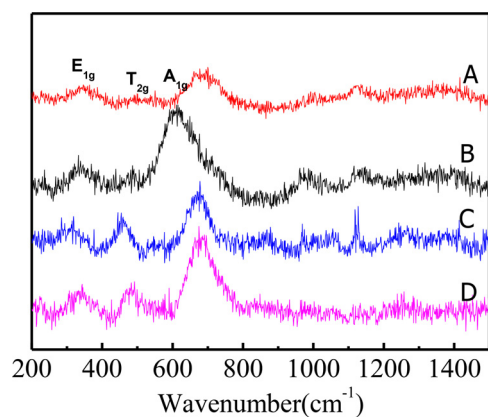


Fig. 3. Raman spectra of ferrites: (A) Fe₃O₄; (B) Fe-Mn; (C) Fe-Co; (D) Fe-Ni.

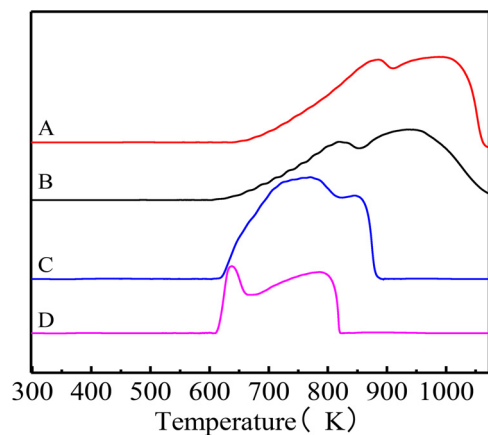


Fig. 4. TPR profiles of Fe-M ferrites: (A) Fe₃O₄; (B) Fe-Mn; (C) Fe-Co; (D) Fe-Ni.

and Fe-Mn. From room temperature (RT) to 350 °C, the peaks at 44.6° became narrower and sharper. However, the peaks of spinel Co_xFe_{3-x}O₄ phase disappeared when reduced at 350 °C for 2 h. In contrast, Fe-Co alloy was generated at the beginning of reduction at 350 °C. Only Fe-Co alloy phase existed after reduction for 5 h. The reduction of Fe-Ni ferrite is shown in Fig. 5(d). The trend depicted is similar to that of the Fe-Co ferrite in that the spinel phase was reduced to Fe-Ni alloy. Moreover, a metallic Fe⁰ phase was also detected apart from an Fe-Ni alloy phase, because Fe-Ni ferrite is easier to reduce than other Fe-M (M = Fe, Mn, Co) ferrites. From the results of *in situ* XRD, we conclude that the degree of reduction for Fe-M (M = Mn, Co, Ni) ferrite under a H₂ atmosphere follows the order Fe-Ni > Fe-Co > Fe₃O₄ > Fe-Mn. This sequence is in agreement with the TPR results.

3.4. XRD patterns of spent Fe-M ferrite

After the FTO reaction, the phase composition of the spent catalyst was determined by XRD (Fig. 6). The peaks ranging from 38° to 60° are assigned to iron carbides, which are generally considered to be the active site for the FTS reaction. For the spent Fe₃O₄ sample, the main phases are Fe₃O₄ and χ -Fe₅C₂, and, for the spent Fe-Mn sample, there are four main phases, namely Fe₃O₄, Mn_xFe_{3-x}O₄, χ -Fe₅C₂, and ϵ -Fe₂C. For the spent Fe-Co sample, Fe-Co alloy, θ -Fe₃C, and χ -Fe₅C₂ are the main phases. For the spent Fe-Ni, there are two phases, Fe-Ni alloy and χ -Fe₅C₂.

3.5. Discussion

Based on the results of the *in situ* XRD in the reduction process and on the XRD patterns of the spent-sample XRD, the structural evolution is summarized in Table 3. The particle size of the reduced samples was calculated using the TOPAS Rietveld refinement software. From the phase analysis of the XRD results, all the spent catalysts contain χ -Fe₅C₂. However, the types of iron carbides are different. For the Fe-Mn spent sample, another kind of carbonaceous species, ϵ -Fe₂C, was detected. Raupp [34] studied the influence of particle size on carbide performance, and found that the smaller particles are favorable to the formation of ϵ -Fe₂C phase. From the grain size of the reduced Fe-Mn sample, we find that grain size of Mn_xFe_{1-x}O is 9.3 nm. Therefore, we speculate that the smaller size of Mn_xFe_{1-x}O is responsible for the production of ϵ -Fe₂C. Otherwise, the conversion of Mn_xFe_{3-x}O₄ to χ -Fe₅C₂ was restrained to some degree compared with the Fe₃O₄ sample, from the quantitative results. For the spent Fe-Mn catalyst, the content of iron carbide is 50.5%, and the content for the spent Fe₃O₄ samples is 71.4%. For the spent Fe-Co catalysts, large parts of the Fe-Co alloy were converted to iron carbide (θ -Fe₃C and χ -Fe₅C₂), and the total content of iron carbide was above 85%. From the components of the spent Fe-Ni sample, it is difficult for the Fe-Ni alloy to be converted to iron carbide. The χ -Fe₅C₂ in the spent sample was mainly converted from the Fe⁰ of the reduced Fe-Ni sample. Raupp [34] also concluded that the Ni can restrain the formation of iron carbide because of the formation of Fe-Ni alloy.

We also find from the XRD pattern of spent samples that there was more deposited carbon in the spent Fe-Mn and Fe-Co samples. The broad peak at approximately 26° corresponding to deposited carbon is attributed to the high CO dissociation ability of Fe-Mn and Fe-Co ferrites. Some active sites of Fe-Mn and Fe-Co are covered by graphitic carbon, which may contribute to the decrease of the CO conversion. We also find from Table 3 that the sizes of the reduced samples were larger than 15 nm, except for Mn_xFe_{1-x}O. De Jong's group [16] has proved that iron particle sizes larger than 15 nm do not play a dominant role in the FTO reaction. This can also explain why the CO conversion of Fe-Ni is the lowest. From TPR and *in situ* XRD results, the Fe-Ni ferrite is easiest to reduce to Fe-Ni alloy and Fe⁰ phase. From the components of the spent Fe-Ni sample, there is relatively little iron carbide generated from the alloy phase. The decreased conversion is explained by taking

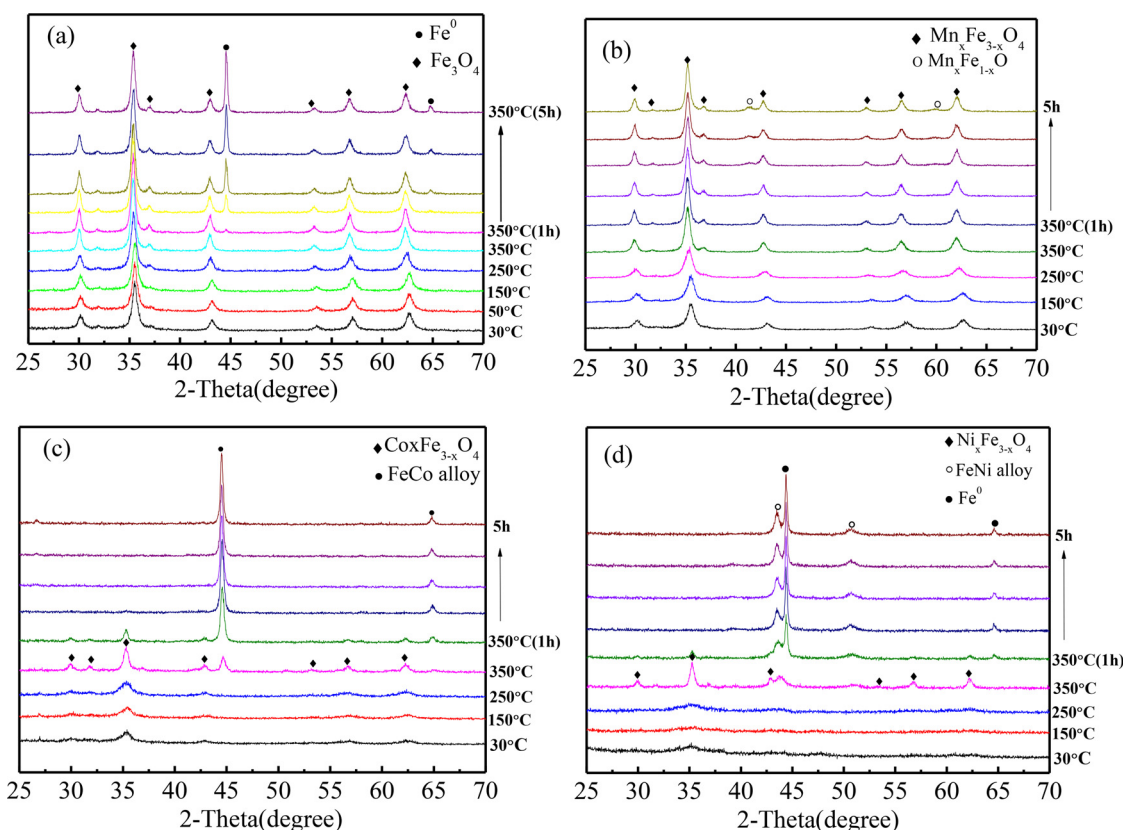


Fig. 5. *in situ* XRD patterns of Fe-M ferrites: (a) Fe_3O_4 ; (b) Fe-Mn; (c) Fe-Co; (d) Fe-Ni.

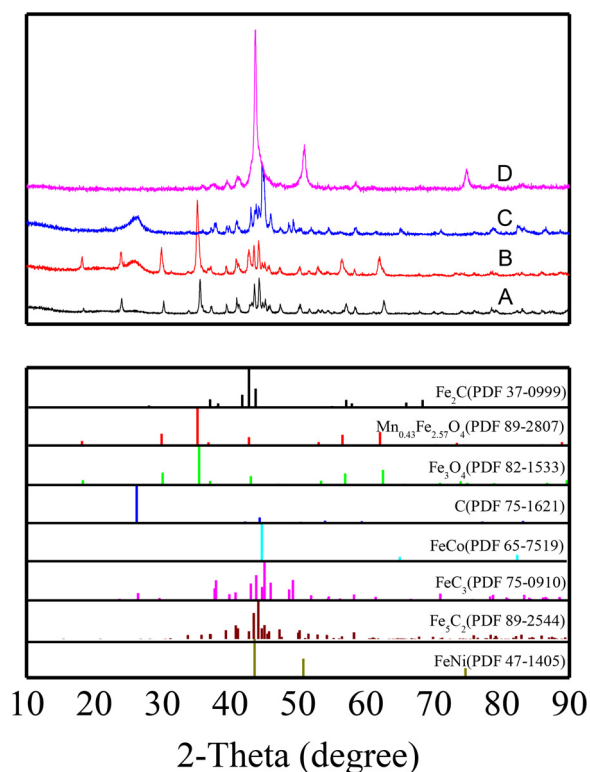


Fig. 6. XRD patterns of spent Fe-M ferrites: (A) Fe_3O_4 ; (B) Fe-Mn; (C) Fe-Co; (D) Fe-Ni.

into account the lower activity of Ni. Therefore, Co and Ni mainly supply a synergistic effect as bimetallic catalysts instead of a main

active phase [6].

As stated above, Mn can suppress the reduction of Fe_3O_4 to Fe^0 , which is considered much easier to carbonize to $\chi\text{-Fe}_5\text{C}_2$ than Fe_3O_4 [35]. Previous research has shown that the $\text{Mn}_x\text{Fe}_{1-x}\text{O}$ phase was responsible for the formation of smaller clusters of $\varepsilon\text{-Fe}_2\text{C}$, which were more active and more selective towards olefins than $\chi\text{-Fe}_5\text{C}_2$ carbide [35,36]. Therefore, the $\varepsilon\text{-Fe}_2\text{C}$ phase may play an important role in enhancing the selectivity of light olefins. CO_2 selectivity of Fe-Mn increases because the main phase of the catalyst is as stable as Fe_3O_4 , which is generally accepted as an active phase of WGS [37]. As demonstrated by the XRD results for the spent catalysts (Fig. 6), most of the carbon species is $\chi\text{-Fe}_5\text{C}_2$, which is active for CO hydrogenation [38]. Hydrogen's activation ability was expected to play a vital role in determining the product distribution. The Fe-Ni system is selective for paraffin formation because of the excess of adsorbed hydrogen [16]. Moreover, the ability of H_2 adsorption over metal is much stronger than that of metal oxide [39]. Fe-Co and Fe-Ni are both reduced to alloys whose hydrogen adsorption ability is much stronger, so it is easier for H_2 to be adsorbed on the surface of Fe-Co and Fe-Ni, which contributes to the promotion of CH_4 and the suppression of chain growth. There is no Fe_3O_4 phase for Fe-Co and Fe-Ni, so the selectivity of CO_2 decreases.

4. Conclusions

In summary, the structural evolution of Fe-M proceeds as follows. For the Fe_3O_4 sample, the phases in the reduced samples were Fe_3O_4 (77.2%) and Fe^0 (22.8%). After the reaction, a large part of the Fe_3O_4 and all of the Fe^0 was converted to $\chi\text{-Fe}_5\text{C}_2$ (71.4%), and a portion of Fe_3O_4 (28.6%) remained in the spent samples. For the Fe-Mn sample, the phases in the reduced sample were $\text{Mn}_x\text{Fe}_{3-x}\text{O}_4$ (73.2%) and $\text{Mn}_x\text{Fe}_{1-x}\text{O}$ (26.8%). In addition to two kinds of iron oxides and $\chi\text{-Fe}_5\text{C}_2$, a new phase, $\varepsilon\text{-Fe}_2\text{C}$, was also detected. $\varepsilon\text{-Fe}_2\text{C}$ may be converted from $\text{Mn}_x\text{Fe}_{1-x}\text{O}$. For the Fe-Co sample, the spinel structure was wholly

Table 3
Overview of components of reduced and spent samples.

Samples	Reduced samples			Spent samples	
	Phase	Grain size (nm)	Percentage (%)	Phase	Percentage (%)
Fe ₃ O ₄	Fe ₃ O ₄	23.3	77.2	Fe ₃ O ₄	28.6
	Fe ^o	77.7	22.8	χ-Fe ₅ C ₂	71.4
Fe-Mn	Mn _x Fe _{3-x} O ₄	22.3	73.2	Mn _x Fe _{3-x} O ₄	45.9
	Mn _x Fe _{1-x} O	9.3	26.8	Mn _x Fe _{1-x} O	3.6
Fe-Co	Fe-Co alloy	50.0	100	χ-Fe ₅ C ₂	42.3
				ε-Fe ₂ C	8.2
				Fe-Co alloy	14.7
Fe-Ni	Fe-Ni alloy	16.5	59.7	θ-Fe ₃ C	44.6
				χ-Fe ₅ C ₂	40.7
				Fe-Ni alloy	49.7
	Fe ^o	71.0	40.3	χ-Fe ₅ C ₂	50.3

reduced to Fe-Co alloy. Then, a large part of the Fe-Co alloy was converted to χ-Fe₅C₂ and θ-Fe₃C. For the Fe-Ni sample, Fe^o phase was found in addition to Fe-Ni alloy phase. The phase of the spent sample then contained χ-Fe₅C₂ and Fe-Ni alloy.

Considering the spinel structure a precursor, the reduction degree under a H₂ atmosphere at 350 °C for 5 h follows the order Fe-Ni > Fe-Co > Fe₃O₄ > Fe-Mn. Both Fe-Ni and Fe-Co form alloys, while Fe₃O₄ and Fe-Mn remain the spinel structure. Furthermore, the reduction state of the catalysts has a series of influences on further Fischer-Tropsch reaction. The reduction state can further influence the carburization of iron. The χ-Fe₅C₂ phase mainly generates the hydrocarbons, but ε-Fe₂C phase plays a vital role in enhancing the selectivity to light olefins. The Fe-Ni and Fe-Co are reduced to alloys, which increase the adsorption and dissociation of H₂ and increases, in turn, the hydrogenation and decrease chain growth. Thus, the selectivity of CH₄ follows the order Fe-Ni > Fe-Co > Fe₃O₄ > Fe-Mn. Fe-Mn and Fe₃O₄ remain of spinel phase, which is the active site of WGS, so the selectivity of CO₂ follows the order Fe-Mn > Fe₃O₄ > Fe-Co > Fe-Ni.

Acknowledgments

The authors are grateful to the support from the National Science Foundation (21406062), the Fundamental Research Funds for the Central Universities (22A201514007). We would like to thank LetPub (www.letpub.com) for providing linguistic assistance during the preparation of this manuscript.

References

- [1] H.M. Torres Galvis, J.H. Bitter, C.B. Khare, M. Ruitenbeek, A.I. Dugulan, K.P. de Jong, *Science* 335 (2012) 835–838.
- [2] A. Corma, F.V. Melo, L. Sauvanaud, F. Ortega, *Catal. Today* 107–108 (2005) 699–706.
- [3] B. Dudley, BP Statistical Review of World Energy, London, UK (2012).
- [4] X.P. Zhou, J. Ji, D. Wang, X.Z. Duan, G. Qian, D. Chen, X.G. Zhou, *Chem. Commun.* 51 (2015) 8853–8856.
- [5] H.T. Galvis, J. Bitter, T. Davidian, M. Ruitenbeek, A. Dugulan, K. de Jong, *J. Am. Chem. Soc.* 134 (2012) 16207–16215.
- [6] H.M. Torres Galvis, K.P. de Jong, *ACS Catal.* 3 (2013) 2130–2149.
- [7] A.Y. Khodakov, W. Chu, P. Fongarland, *Chem. Rev.* 107 (2007) 1692–1744.
- [8] J.M.G. Carballo, E. Finocchio, S. García-Rodríguez, M. Ojeda, G. Busca, S. Rojas, *Catal. Today* 214 (2013) 2–11.
- [9] E. Iglesia, S.L. Soled, R.A. Fiato, *J. Catal.* 137 (1992) 212–224.
- [10] R.A. Dictor, A.T. Bell, *J. Catal.* 97 (1986) 121–136.
- [11] C.K. Rofer-Depoorter, *Chem. Rev.* 81 (1981) 447–474.
- [12] N. Lohitharn, J.G. Goodwin, E. Lotero, *J. Catal.* 255 (2008) 104–113.
- [13] H. Xiong, M. Moyo, M.A.M. Motchelaho, L.L. Jewell, N.J. Coville, *Appl. Catal. A: Gen.* 388 (2010) 168–178.
- [14] Y. Jin, A.K. Datye, *J. Catal.* 196 (2000) 8–17.
- [15] D. Duvenhage, N. Coville, *Appl. Catal. A: Gen.* 233 (2002) 63–75.
- [16] T. Ishihara, K. Eguchi, H. Arai, *Appl. Catal.* 30 (1987) 225–238.
- [17] M. Feyzi, A.A. Mirzaei, *J. Natl. Gas Chem.* 19 (2010) 422–430.
- [18] F. Tihay, A. Roger, A. Kiennemann, G. Pourroy, *Catal. Today* 58 (2000) 263–269.
- [19] S.A. Al-Sayari, *Ceram. Int.* 40 (2014) 723–728.
- [20] H.M. Torres Galvis, J.H. Bitter, T. Davidian, M. Ruitenbeek, A.I. Dugulan, K.P. de Jong, *J. Am. Chem. Soc.* 134 (2012) 16207–16215.
- [21] Y. Zhang, Long. Ma, T. Wang, X. Li, *New. J. Chem.* 39 (2015) 8928–8932.
- [22] J. Wei, J. Sun, Z. Wen, C. Fang, Q. Ge, H. Xu, *Catal. Sci. Technol.* 6 (2016) 4786–4793.
- [23] Y.L. Zhang, L. Ma, T.J. Wang, X.J. Li, *RSC Adv.* 5 (2015) 45426–45430.
- [24] B.F. Shi, J.W. Ren, X.H. Liu, G.Z. Lu, Y.Q. Wang, *Synth. Met.* 162 (2012) 1443–1450.
- [25] H. Deng, X. Li, Q. Peng, X. Wang, J. Chen, Y. Li, *Angew. Chem. Int. Ed.* 44 (2005) 2842–2845.
- [26] H. Lai, Z. Zhang, F. Gu, Z. Yi, Z. Zhong, F. Su, *RSC Adv.* 5 (2015) 13374–13384.
- [27] W. Wang, Z. Ding, X. Zhao, S. Wu, F. Li, M. Yue, J.P. Liu, *J. Appl. Phys.* 117 (2015) 17A328.
- [28] R. Pazik, E. Piasecka, M. Malecka, V.G. Kessler, B. Idzikowski, Z. Sniadecki, R.J. Wiglus, *RSC Adv.* 3 (2013) 12230–12243.
- [29] H.C. Choi, Y.M. Jung, S.B. Kim, *Vibr. Spectrosc.* 37 (2005) 33–38.
- [30] F. Tihay, A. Roger, G. Pourroy, A. Kiennemann, *Energy Fuels* 16 (2002) 1271–1276.
- [31] Y. Liu, J.-F. Chen, J. Bao, Y. Zhang, *ACS Catal.* 5 (2015) 3905–3909.
- [32] M. Ding, Y. Yang, B. Wu, Y. Li, T. Wang, L. Ma, *Appl. Energy* 160 (2015) 982–989.
- [33] F. Gao, H. Wang, M. Qing, Y. Yang, Y. Li, *Chin. J. Catal.* 34 (2013) 1312–1325.
- [34] G.B. Raupp, W.N. Delgass, *J. Catal.* 58 (1979) 337–347.
- [35] J.F. Bengoa, A.M. Alvarez, M.V. Cagnoli, N.G. Gallegos, S.G. Marchetti, *Appl. Catal. A: Gen.* 325 (2007) 68–75.
- [36] A. Campos, N. Lohitharn, A. Roy, E. Lotero, J.G. Goodwin, J.J. Spivey, *Appl. Catal. A: Gen.* 375 (2010) 12–16.
- [37] M. Luo, H. Hamdeh, B.H. Davis, *Catal. Today* 140 (2009) 127–134.
- [38] T. Herranz, S. Rojas, F.J. Pérez-Alonso, M. Ojeda, P. Terreros, J.L.G. Fierro, *J. Catal.* 243 (2006) 199–211.
- [39] G.H. Guvelioglu, P. Ma, X. He, R.C. Forrey, H. Cheng, *Phys. Rev. Lett.* 94 (2005) 026103.